NJC

ROYAL SOCIETY OF CHEMISTRY

PAPER

View Article Online
View Journal | View Issue

Cite this: *New J. Chem.*, 2021, **45**, 16594

Surface and morphological studies of $LiNbO_3$: p-type semiconductivity on stoichiometric surfaces

Luis Henrique da Silveira Lacerda, *[a] Miguel Angel San-Miguel [a] and Sergio Ricardo de Lazaro [b]

Received 17th May 2021,
Accepted 3rd August 2021

DOI: 10.1039/d1nj02429a

rsc.li/njc

$LiNbO_3$ is a semiconductor material employed in the development of several technological devices and processes. However, its suitability is expanded when p-type semiconductivity is obtained. In this work, density functional theory (DFT) simulations using the B3LYP hybrid functional connect the surface and crystalline morphology of $LiNbO_3$ to its semiconductivity features. Thus, the main low-index surfaces were carefully investigated, presenting the influence of O vacancies on surface stability and structural and electronic features. The results also illustrate the electronic properties of surfaces in terms of band gap, charge carrier stability, and semiconductor type, the latter being dependent on the surface direction. Finally, a large set of possible crystalline morphologies for $LiNbO_3$ is presented, predicting the expected properties for different crystal shapes from the calculated surface properties. A particular behavior is found observing the existence of both p- and n-type semiconductivity in the same morphology.

Introduction

The investigation of solid-state materials is strongly connected to technological advances. Thus, semiconductors, photonic materials, magnetic materials, catalysts, ferroelectric materials, piezoelectric materials, and other types of solid-state materials were deeply investigated over the years. Among the materials with high technological potential, lithium niobate ($LiNbO_3$) stands out as a wide band gap semiconductor with a unique set of photonic, photoacoustic, pyroelectric, thermoelectric, piezoelectric, and ferroelectric properties.[1–8]

The first $LiNbO_3$ study took place over 70 years ago. To the best of our knowledge, the first manuscript was published in 1943 by Matthias and Remeika[9], where $LiNbO_3$ was reported as an ilmenite material. This definition was accepted until 1952, when Bailey[11,14] showed that, under room conditions, the space group is $R3C$ with lattice parameters $a = b \neq c$ and angles $\alpha = \beta = 90^\circ$ and $\gamma = 120^\circ$, exhibiting [LiO_6] and [NbO_6] distorted clusters. This structure is related to high ferroelectric properties raised from highly compacted layers, the distortion of octahedral clusters, the alteration of A and B cations along the c axis, and the presence of intrinsic vacancies.[1,10–14]

$LiNbO_3$ is one of the most exciting candidates for developing integrated photonic devices, acoustic-optical and non-linear-based devices, waveguides, couplers, wavelength converters, and electro-optical modulators.[15–20] The doping process can expand the high suitability of $LiNbO_3$.[2,21] For instance, Fe- and Cu-doping results in photorefractive responses; the Nd-, Yb- and Er-doping results in active features for laser generation.[21] In both cases, the resulting materials are potential alternatives to developing holographic storage devices or laser gain media.[2,8] In turn, Mg- and Zn-doped $LiNbO_3$ enable the production of photodamage-resistant wafers.[21] The main limitation to the application of $LiNbO_3$ lies in the absence of p-type semiconductivity responsible for its use as a passive component of important devices. Thus, thermoelectric oxidation, ultraviolet irradiation, and intense doping processes with optical damage resistant species were carried out to produce p-type $LiNbO_3$.[22–25] Recent reports suggest that N-doping can produce $LiNbO_3$ materials with p-type semiconductivity.[26,27]

The conduction mechanism of $LiNbO_3$ depends on structure, stoichiometry, temperature, and synthesis conditions. Hence, beyond n- or p-type semiconductivity, recent studies report[20,28,29] the polaronic conductivity as the dominating charge transport mechanism in $LiNbO_3$, mainly for high temperatures.[30] It is generally accepted that the defects are responsible for small polaron or bipolaron formation by trapping electrons at one structure site.[20,31–33]

In recent years, $LiNbO_3$ has been extensively investigated. Levchenko and Rappe[34] reported a broad theoretical investigation of the (0001) surface predicting the relative thermodynamic stability of this surface considering different non-stoichiometric surface compositions. Similarly, Sanna and Schmidt[35] have investigated the $(21\bar{1}0)$, $(1\bar{1}00)$, and (0001) non-stoichiometric surfaces describing the influence of surface structure, surface stoichiometry, and chemical potentials of Li, Nb, and O species

[a] *State University of Campinas, Campinas, São Paulo, Brazil. E-mail: lhslacerda1@gmail.com*
[b] *State University of Ponta Grossa, Ponta Grossa, Paraná, Brazil*

on ferroelectric polarization. Another work by Sanna and Schmidt[36] consists of a careful revision of experimental and theoretical results regarding the $LiNbO_3$ surfaces. In this work, the authors discuss the determination of surface formation energies, the thermodynamic features of surfaces with different stoichiometry, and phase diagrams containing different surfaces. Furthermore, other theoretical studies focusing on non-stoichiometric surfaces have been published.[37–41] In the context of morphological studies, some relevant DFT studies presenting morphologies mainly composed of $(2\bar{1}\bar{1}0)$, $(1\bar{1}00)$, and (0001) surface cuts can be found in ref. 42 and 43. Furthermore, the calculated surface energies for the (001), (010), and (100) surfaces were employed to create a possible morphology for $LiNbO_3$ crystals.[44]

The main contribution of our manuscript to the literature lies in the evaluation of stoichiometric surfaces of $LiNbO_3$ since most articles focus on non-stoichiometric surface models. In this work, we perform a careful DFT/B3LYP investigation connecting the surface and morphological properties of $LiNbO_3$ to its semiconductivity. In the first section of the results, the structural features of surfaces were discussed in terms of surface energies and stability, evaluating the coordination number of cations and density of defects. In addition, the electronic properties of $LiNbO_3$ surfaces were carefully investigated, presenting electronic structures, band gap values, and electron and hole charge carrier concentrations and stability. In turn, the second section of the results exhibits a large set of available morphologies for the investigated material depicting their expected properties. In summary, the results pave the way to tune the semiconductivity type observed in materials as $LiNbO_3$ by controlling the crystal morphology.

Computational details

This work evaluates the surface and morphological properties of $LiNbO_3$ in the *R*3*c* crystalline structure using a slab construction model. This model results from the assessment of two-dimensional periodic models composed of atomic layers parallel to the (*hkl*) planes "cutting out" from the previously full-relaxed bulk structure with no imaginary frequencies. Based on the X-ray diffraction (XRD) results reported by Schirmer *et al.*[1] and confirmed by Zotov *et al.*,[45] the low index surfaces (001), (101), (110), (100), (012), and (111) were examined. In particular, the (110) surface is non-polar, while the (001), (101), (100), (012), and (111) surfaces are polar surface outcrops, according to Tasker's classification.[46] The main difference between both surface groups lies in the macroscopic dipole moment (μ_Z). A $\mu_Z = 0$ is connected to a non-polar surface and $\mu_Z \neq 0$ is observed for polar surfaces.

A layer (slab) growth was carried out for all surface directions. The growth is performed by adding further atomic layers, preserving the $LiNbO_3$ stoichiometry, to test the convergence of the surface energy regarding the slab thickness. Furthermore, growth is mandatory for polar surfaces due to the macroscopic dipole and its influence on obtaining converged calculations. Thus, a widely used strategy is to grow the surface model until the surface energy values converge. This simple methodology does not require chemical adsorption or surface reconstruction to cancel the macroscopic dipole.[47,48] The first step consists of the calculation of the unrelaxed cleavage energy (γ^{unrelax}) from two complementary terminations using eqn (1). The unrelaxed surface termination is divided into upper (T_U) and down (T_D) terminations. $E_{\text{slab}}^{\text{unrelax}}$ and E_{bulk} refer to the total energies for the unrelaxed model and the bulk unit, respectively; n is the number of bulk units and A is the surface area.

$$\gamma^{\text{unrelax}} = \frac{(E_{\text{slab}}^{\text{unrelax}} - nE_{\text{bulk}})}{2A}. \quad (1)$$

The next step for the polar surface study refers to the relaxation of the complementary terminations (T_U and T_D). Therefore, the energy for relaxed surfaces (γ) is computed by eqn (2).

$$\gamma = \frac{(E_{\text{slab}}^{\text{relax}} - nE_{\text{bulk}})}{2A}. \quad (2)$$

It is essential to highlight that this methodology takes into account the internal polarization raised within the surface and its influence on the surface energy and structural properties. The increase of surface thickness is also responsible for the minimization of the macroscopic dipole in polar surfaces.

Table 1 summarizes each stabilized surface feature in terms of layer composition in each minimal surface unit, surface type, thickness (in layers), and area. As previously mentioned, the progressive thickness increase of the surface models is performed until the convergence of surface energy values is achieved for each surface direction. From the calculated cleavage energies (Table 2), it is possible to describe the energy cost to create a distinct surface taking into account the breakage of chemical bonds and changes in the coordination numbers of atoms on the surface. The methodology employed in this work is very representative and already successfully predicted the surface properties of several materials.[49–55] Although this methodology is a zero-temperature and zero-pressure technique, it has been extensively used to predict the surface properties and morphologies of several materials successfully.[49–55] To model the effects of experimental conditions with temperature and pressure different from zero, it is possible to use *ab initio* thermodynamics approaches, in which the chemical potentials (μ) of each participating species must be included.[48,56–58] However, these studies are far from the scope of this work since we focus on stoichiometric surfaces.

Table 1 Surface composition, surface polarity, thickness (in layers), and area (Å^2) for low index surfaces evaluated for $LiNbO_3$. The surface direction investigated is presented here using Miller- and Miller–Bravais notations

Miller notation	Miller–Bravais notation	Surface composition	Polarity	Thickness	Area
001	0001	Nb–O_3–Li–Nb–O_3–Li	Polar	12	23.307
012	$01\bar{1}2$	Nb_2–O_2–O_2–Li_2–O_2	Polar	10	28.858
100	$10\bar{1}0$	O_4–Li_2–Nb_2–O_2	Polar	12	72.954
101	$10\bar{1}1$	O–Nb–O–Li–O_2–Nb–O–Li–O	Polar	20	25.529
110	$11\bar{2}0$	O_3–Li_2–Nn_2–O_3	Non-polar	21	42.120
111	$11\bar{2}1$	O–Nb–O_2–Li–O_2–Nb–O–Li	Polar	50	128.492

In this manuscript, all simulations considered the models under vacuum and zero Kelvin using a DFT/B3LYP[59] approach in the CRYSTAL17 quantum code.[60] The 8-411,[61,62] 5-11(1d)G,[63] and HAYWSC-31(31d)G[63] basis sets described the O, Nb, and Li atoms, respectively. Furthermore, the employment of a high-level self-consistent field (SCF) parameterization guaranteed excellent reliability for our results. The SCF convergence truncated in 10^{-8}, Monkhorst–Pack[64,65] methods defined as $8 \times 8 \times 8$, the Coulomb and exchange integral calculations controlled by five thresholds set to 10^{-7}, 10^{-7}, 10^{-7}, 10^{-7}, and 10^{-14} Ha, and the convergence criteria for mono- and bi-electronic integrals set to 10^{-8} Ha determine the high-level SCF parametrization. The Fermi energy levels for the investigated $LiNbO_3$ surfaces were obtained from DFT calculations using a hybrid exchange–correlation functional (B3LYP). The Fermi level is automatically provided by the CRYSTAL quantum code from the Fermi distribution.

Results and discussion

Surface properties

The $LiNbO_3$ structure (Fig. 1) is characteristically observed with the *R*3*c* space group. The surfaces investigated were obtained from slab cuts along low index directions and were evaluated in terms of structural and electronic properties.

Initially, we discuss the structural features. Fig. 1 presents the fully relaxed surfaces depicting each surface composition and the number of vacancies (coordination number) of each cation in a specific cut. Table 2 exhibits the unrelaxed cleavage energy ($\gamma^{unrelax}$) and the surface energy (γ) for relaxed surfaces. The evaluation of γ values indicates that the stability of the $LiNbO_3$ surface decreases in the following order (012) > (101) > (110) > (001) > (100) > (111). In summary, the density of defects influences the surface energy since a low atomic coordination number (*i.e.*, high number of vacancies) is connected to high surface energy.[51,55] This influence is caused by the number of Nb–O and Li–O bonds that should be dangled to obtain the slab cut. Consequently, the number of dangling bonds represents the number of oxygen vacancies (V_O^X) formed regarding the initial coordination in the bulk.

The (012) surface is the most stable, showing Li atoms exposed on T_U and O atoms on T_D. In both terminations, $[LiO_5]$ and $[NbO_5]$ clusters are observed with one O vacancy. The low surface energy values for the (012) surface are reliable indicators of the flexibility of Li–O and Nb–O bonds, enabling surface energy minimization. In turn, the surface energy for other surfaces changes as a function of the density of defects and surface termination type.

A direct comparison between the surface energy for the (100) and (001) surfaces shows that the chemical composition of the termination has more influence on the surface energy than the density of defects. Therefore, it is expected that O-terminated surfaces are more stable than cation-terminated surfaces with a minor number of vacancies. Furthermore, the simultaneous existence of Nb and Li occupying sites with different coordination numbers in the (100) and (111) surfaces breaks the bulk symmetry increasing the surface energy values.[1,66–69]

All the electronic properties of surface models were evaluated by the density of states (DOS), band structure, charge carrier mobility, and semiconductivity type. Fig. 2 shows the total projected DOS. For (101), (001), (012), (100), and (110) surfaces, the valence band (VB) is almost entirely composed of O states with a low contribution of Nb atoms. The (111) surface presents the lowest energy region of VB composed of O states, being the top of the VB majorly composed of Nb states. In turn, the conduction band (CB) for all surfaces has a major contribution of Nb states allied to the significant participation of O atoms. The Li states present a substantial contribution to the top of the VB and the bottom of the CB.

Fig. 2 shows the band structure profiles. For (001) and (111) surfaces, the energy levels of VB and CB are well-spaced in terms of energy. The energy difference between levels composing VB or CB decreases for (012), (101), and (110) surfaces, being the energy levels closer to each other for the two surfaces previously mentioned. Meanwhile, the energy levels of CB and VB for the (100) surface are very close to each other. Moreover, the flat band is observed for at least one energy level on all the surfaces; and more interestingly, the (111) surface presents six flat bands. The existence of flat bands can be understood as energy levels that behave like atomic energy levels since they have suffered a small perturbation from the interaction with neighbor atoms due to vacancies. Therefore, the high density of structural defects within the (111) surface is reflected in an increased number of flat bands.

In simple and complex oxide materials with the typically semiconductor band gap, such as ZnO, TiO_2, and others, the semiconductivity type is determined by the main type of charge carrier that dominates the conduction process. Then, the materials and surfaces are classified as n-type or p-type semiconductors when electrons or holes are predominant in the conduction process, respectively.[70,71]

In this work, two different approaches have been employed to predict the charge carrier concentration on $LiNbO_3$ surfaces. The first methodology consists of integrating the VB or CB areas

Table 2 Calculated values for unrelaxed cleavage energy ($\gamma^{unrelax}$), energy (γ), coordination number for Li and Nb atoms (CN), and oxygen vacancies number (V_O^X) for the low index surfaces (110), (001), (012), (100), (101), and (111) on the upper and down terminations (T_U and T_D). The surface energy values are in J m^{-2}

					CN		Defects
Surface	$\gamma^{unrelax}$	γ	Terminations		Li	Nb	V_O^X
(012)	3.611	1.080	T_U	Li_2–O	5	—	1
			T_D	Nb_2–O	—	5	1
(101)	3.405	1.324	T_U	O–Nb–O	—	4	2
			T_D	O–Li–O	2	—	4
(110)	2.595	1.520	T_U	O–O–O–Li	2	—	4
			T_D	Nb–O–O–O	—	5	1
(001)	4.807	1.554	T_U	Nb–O	—	6	0
			T_D	O–Li	3	—	3
(100)	4.291	2.123	T_U	O–O–Li	1	—	5
			T_D	Li–Nb–O	3	4	5
(111)	5.234	3.097	T_U	O–Nb–O	—	4	2
			T_D	Nb–O–Li	4	3	5

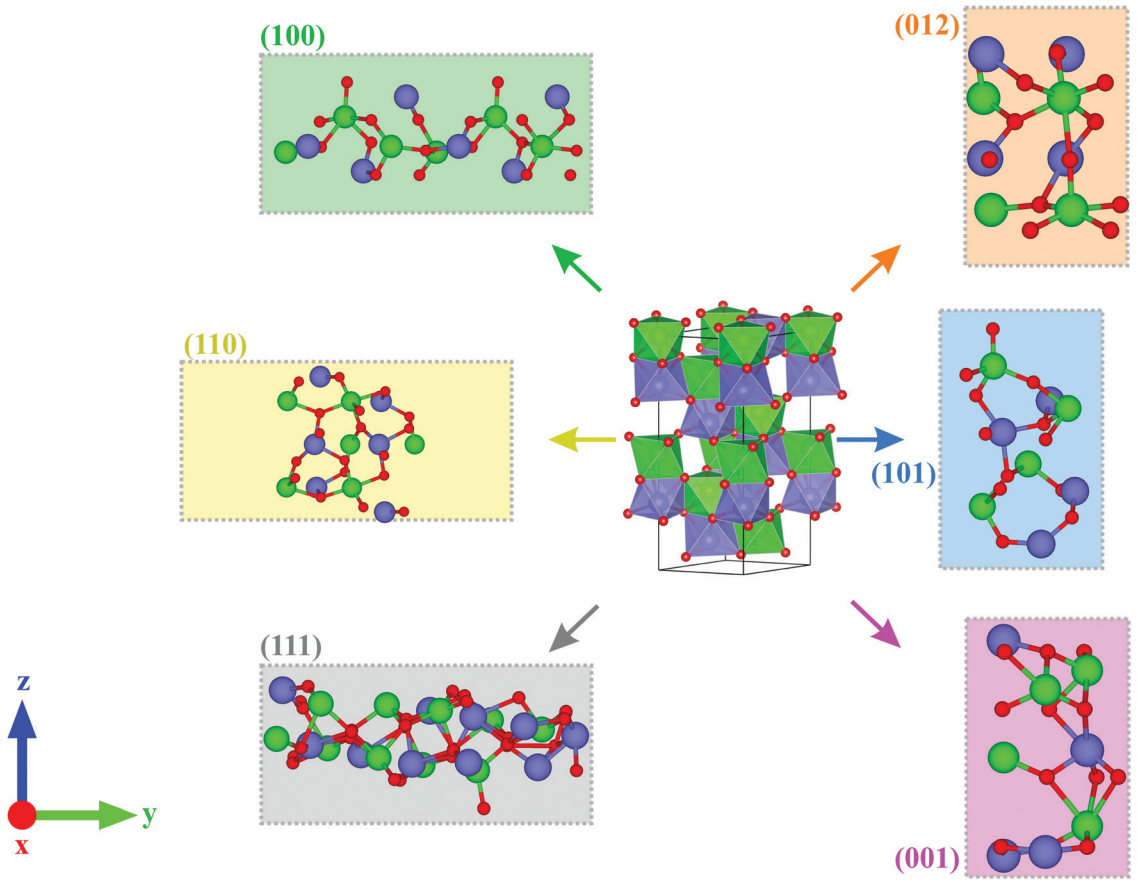

Fig. 1 Relaxed surface slabs for $LiNbO_3$. The lilac, green, and red spheres (polyhedra) represent the Li, Nb, and O atoms, respectively.

in the DOS (obtained from the Simpson 1/3 rule[72]) divided by unit cell or surface volume, resulting in values expressed in terms of states/cm^3. The resulting values for VB and CB represent the number of available states to rising holes ($h^\bullet$) and electrons (e^-), respectively. This methodology has been used in different studies, providing reliable results in agreement with the experimental evidence from Hall effect techniques and other theoretical approaches.[73–77] A higher number of states in the VB (holes) is characteristically associated with p-type semiconductors, whereas the n-type semiconductor has an increased number of states in the CB (electrons). In semiconductors, the conduction process is controlled by the charge carrier on a higher amount; thus, the conduction process on p-type semiconductors occurs predominantly by holes, while the electrons are the predominant charge carrier on the conduction process for n-type semiconductors.

The results for $LiNbO_3$ surfaces (Table 3) show that only the (111) surface presents n-type behavior, the same semiconductivity type as observed for the bulk in our calculations and other studies.[2,20] The other surfaces are p-type semiconductors. This fact is confirmed by the major contribution of the O atoms in the VB, favoring the positive charge accumulation on the surface. Wang *et al.*[27] reported a similar behavior caused by doping with non-metallic species. Another valuable comment lies on the individual mobility of charge carriers that can be accessed from effective mass values for electrons (m_{e^*}/m_o) and holes (m_{h^*}/m_o). It is known that high mobilities are expected for charge carriers with low mass values.[78,79] Thus, the calculated values for the $LiNbO_3$ bulk and surfaces indicate that only the bulk form and (012), (101), and (100) surfaces present the predominant charge carrier with a good mobility. Meanwhile, the other surfaces have the minority charge carrier with better mobility.

Also, materials with the predominant charge carrier of low effective mass present a good efficiency in the conduction process[78] and, therefore, the mentioned surfaces are expected as good efficient semiconductors.

The second approach employed to estimate the charge carrier concentration is the Fermi distribution, which considers the temperature effects on the number of electrons and holes.[78,80] This methodology is a reliable approach to predicting the semiconductor type, as evidenced previously[81–83]. The obtained results for the charge carrier density values at 300 K, 600 K, and 900 K are shown in Table 4. In summary, the results indicate a significant increase in the charge carrier number as the temperature increases, as expected for semiconductors. The results suggest that the conduction processes in the bulk and (111) surfaces are controlled by electrons (n-type), while the other surfaces present p-type semiconductivity. The semiconductivity for the bulk phase is in agreement with experimental results for $LiNbO_3$, but no experimental data for surfaces were found. Furthermore, the results obtained from both methodologies agree with each other

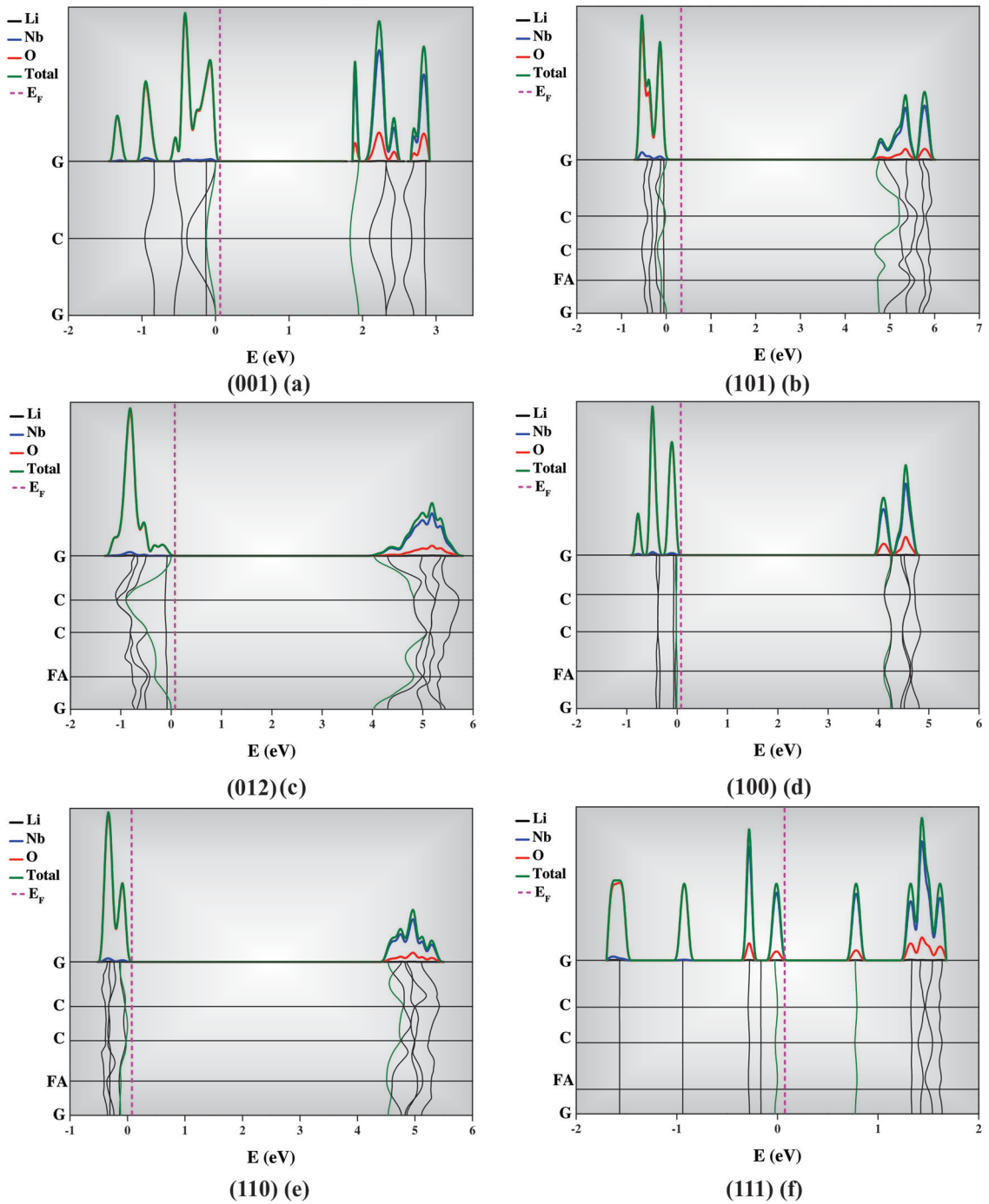

Fig. 2 Total density of states projected and band structures for (001) (a), (101) (b), (012) (c), (100) (d), (110) (e), and (111) (f) surfaces of the $LiNbO_3$ polymorph.

Table 3 Band gap, available states on the top of the valence band (VB) and the bottom of the conduction band (CB), and effective mass for charge carriers on (110), (001), (012), (100), (101), and (111) surfaces of $LiNbO_3$

	Available states (states per cm^3)				Effective masses		
	VB	CB	Semiconductor type	Band gap (eV)	m_{h^*}/m_o	m_{e^*}/m_o	m_{h^*}/m_{e^*}
Bulk	2.99×10^{22}	3.06×10^{22}	n	4.72 (G–G)	15.79	11.57	1.36
(012)	2.57×10^{25}	2.00×10^{25}	p	4.04 (G–G)	4.53	26.29	0.17
(110)	1.72×10^{25}	1.70×10^{25}	p	4.51 (C–G)	102.92	49.71	2.07
(101)	2.37×10^{25}	1.82×10^{25}	p	4.66 (C–C)	8.30	34.84	0.29
(001)	1.57×10^{25}	1.00×10^{25}	p	1.84 (G–C)	61.18	37.32	1.64
(100)	2.71×10^{25}	1.92×10^{25}	p	4.11 (C–C)	25.06	276.70	0.09
(111)	1.97×10^{25}	1.99×10^{25}	n	0.77 (C–CA)	78.40	90.54	0.87

Table 4 Charge carrier density values for the bulk and (110), (001), (012), (100), (101), and (111) surfaces of the $LiNbO_3$ obtained from the Fermi distribution

	Charge carrier density (cm^{-3})					
	300 K		600 K		900 K	
	Holes	Electrons	Holes	Electrons	Holes	Electrons
Bulk	7.448×10^{20}	7.639×10^{20}	$7{,}634 \times 10^{20}$	7.829×10^{20}	8.090×10^{20}	8.296×10^{20}
(012)	2.989×10^{20}	2.329×10^{20}	3.063×10^{20}	2.387×10^{20}	3.247×10^{20}	8.296×10^{20}
(110)	6.630×10^{19}	6.585×10^{19}	6.795×10^{19}	6.750×10^{19}	7.201×10^{19}	7.153×10^{19}
(101)	2.297×10^{20}	1.766×10^{20}	2.354×10^{20}	1.810×10^{20}	2.495×10^{20}	1.918×10^{20}
(001)	1.283×10^{20}	8.216×10^{19}	1.315×10^{20}	8.420×10^{19}	1.394×10^{20}	8.923×10^{19}
(100)	2.519×10^{20}	1.787×10^{20}	2.581×10^{20}	1.831×10^{20}	2.735×10^{20}	1.941×10^{20}
(111)	2.352×10^{19}	2.369×10^{19}	2.411×10^{19}	2.428×10^{19}	2.555×10^{19}	2.573×10^{19}

and with other studies predicting the charge carrier concentration of perovskites and simple and complex oxides.[84]

The investigation of the semiconductivity type for surfaces is fundamental to determine the expected behavior under different conditions. The $LiNbO_3$ is one of the most promising candidates for several applications;[15–19] however, the inexistence of p-type semiconductivity represents a big challenge in $LiNbO_3$ applications. Thus, thermoelectric oxidation, ultraviolet irradiation, and intense doping processes with optical damage resistant species were carried out to produce p-type $LiNbO_3$.[22–25] Recent reports suggest that N-doping can produce $LiNbO_3$ materials with p-type semiconductivity.[26,27] On the other hand, our results indicate that stoichiometric and non-symmetric surface cuts along the (012), (110), (101), (001), and (100) directions create the p-type semiconductivity highly desired for previously mentioned technological applications.

It is noteworthy that DFT methods are certainly adequate to tackle the electronic features of ground states, and the assessment of the semiconductivity type from the number of available charge carriers is related to the excited electronic states. However, several approaches (such as the Fermi rule,[72] the Boltzmann transport approximation[85], localized states evaluation on CB and VB[78], the Simpson 1/3 rule,[72] and the Fermi distribution[78,80]) have predicted the semiconductivity type for diverse materials successfully.

Finally, the electronic properties for the different surface cuts were evaluated in terms of the band gap and charge carrier stability. In summary, the $LiNbO_3$ presents an insulator band gap in the bulk form that remains for (012), (110), (101), and (100) surface cuts. On the other hand, the (001) surface presents a typical semiconductor band gap, whereas the (111) surface presents band gap values characteristic of conductor materials. Thus, these surfaces show high potentials for electronic applications. In particular, the (001) surface is suitable for photocatalytic-based applications. In general, the development of materials for photocatalytic applications aims at materials with a band gap in the visible region of the electromagnetic spectrum (1.6–3.3 eV). It is important to compare our theoretical prediction with experimental measurements that report a wide-semiconductor band gap of 3.8 eV.[86,87] The difference can be justified by the high spontaneity to form defects when synthesized.[1,66,88,89] The same deviation from experimental values was reported by Wang *et al.*[27] using the HSE06 functional. Regarding the surfaces, we expect that our prediction is reliable due to the high density of defects, and consequently, an excellent agreement with experimental approaches.[90]

In turn, the charge carrier stability obtained from effective masses[91–94] was presented in Table 3. The study of the stability of charge carriers is essential to determine the photocatalytic potential since the stable charge carriers are related to high efficiency in the photocatalytic process due to an expected minor recombination rate.[95–98] The stability of the charge carriers (electron–hole pair) was predicted by the ratio between electrons and hole effective masses (m_{h*}/m_{e*}); thus, the values lower than 0.5 or higher than 1.5 indicate a good charge carrier stability and, hence, a low possibility of electron–hole recombination.[95,96,99,100] In other words, the high stability of the charge carriers promotes the migration of e^- and $h^\bullet$, inhibiting their recombination. The obtained results indicate the good stability of the charge carriers for (012), (110), (101), (001), (100), and (111) surfaces. Furthermore, the results confirm the (001) surface as the potential effective photocatalyst and are shreds of evidence of the excellent charge separation for the other mentioned surfaces. Li *et al.*[101] and Sumets[28] report the charge separation experimentally observed. The high stability of the charge carriers is also exciting for thermoelectric applications.[88,102–104]

In summary, our results indicate that the properties of $LiNbO_3$ in the bulk form, desired for photoacoustic and other acoustic applications, are also observed for (012), (110), (101), and (100) surfaces, yielding a high potential for technological applications.

Crystal morphology

Once the surface properties of the main surfaces of $LiNbO_3$ were evaluated, it is possible to predict the available crystal shapes using the Wulff model.[105,106] This methodology employs the γ values for each surface to obtain an ideal morphology. It is feasible to obtain other crystal morphologies by tuning one or more surface energy values from this ideal crystal shape.[107,108] Each surface's contribution to the crystal shape occurs according to its γ values, *i.e.*, low surface energy indicates a high surface contribution. Accordingly, a specific surface contribution can be increased by the decrease of its γ values or *vice versa*.

The Wulff model is a handy approach to predict the possible morphologies of solid-state materials obtained from different synthesis routes or conditions, such as the epitaxial growth, thermal treatment, and others.[107–109] The validity of the method

has been extensively demonstrated[53–55,110,111] and also evidenced in this work when comparing the theoretical morphologies with the experimentally observed SEM images.

A complete set of available morphologies for $LiNbO_3$ (Fig. 3) is obtained. The ideal morphology for $LiNbO_3$ is majorly composed of (012) and (101) surfaces with a not well-defined shape. The first morphology set (labeled as 1) is obtained from the decrease of the (012) surface energy, obtaining perfect-cubic (1.2) and quasi-cubic ((1.1) and (1.3)) shapes. The second set is obtained by tuning the (101) and (001) surface energies resulting in trigonal-plates (2.6), entirely trigonal-faceted (2.5), diamond faces (2.1, 2.2, and 2.4), and irregular trigonal shapes (2.3). The third set is obtained by changes in γ for two different surface cuts. The decrease of the (110) γ creates nanorods (3.4) with hexagonal bases, while the reduction of the (001) γ results in the (3.5) and (3.6) crystal shapes; the latter presents a hexagonal-plate form.

Furthermore, the (4.1) and (4.2) crystal shapes are obtained from the (001) surface energy decrease, while the (5.1), (5.2), (5.3), and (5.4) crystal shapes are achieved by the decrease of the (100) surface. In particular, the crystal shape majorly composed of the (100) surface presents trigonal nanorod shapes (5.4). The last morphology set was obtained from a decrease of the (111) γ, resulting in the crystal shape with a non-regular form (6.1), a concave polyhedral (6.2), a commemorative balloon-like shape (6.3), and a trigonal prism (6.4). It is noteworthy that the fifth and sixth morphological sets present branches obtained from the changes of two or more surface energies.

Although the $LiNbO_3$ has been extensively investigated in the past few decades, the comparison between theoretical morphologies predicted in this work and SEM analysis is not easy. The difficulty lies in the low scanning resolution or not well-defined shapes observed during the experiments.[112–116] Nevertheless, our morphological predictions are in agreement with other experimental results since the ideal polyhedral,[117,118] (1.2),[90] (1.3),[119–122] (2.2),[123] (2.5),[124] (3.5),[119,125] (5.1.1),[118] (5.1.2),[118,121] and (6.4)[36,122,126,127] were already synthesized. As previously commented, such agreement evidences our methodology's reliability in predicting newly available shapes not reported yet for $LiNbO_3$.

Our morphological results enable us to state the potential applications of each crystal shape. For instance, the (6.1), (6.2), (6.3), (6.1.1), and (6.1.2) crystal shapes present a great exposition of the (111) surface. Hence, these morphologies are good

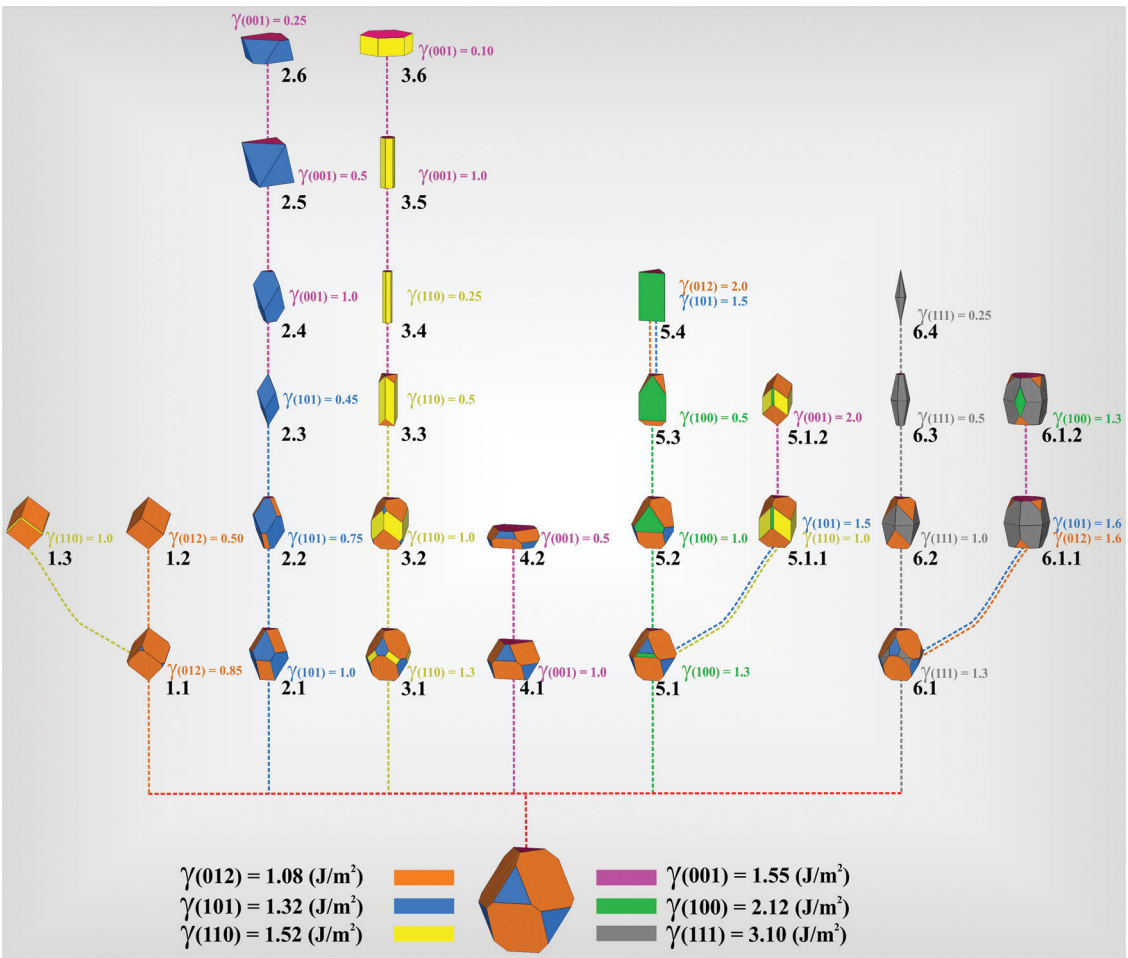

Fig. 3 Complete set of available morphologies for $LiNbO_3$ considering the (110), (012), (101), (100), (001), and (111) surfaces. The colored dashed lines indicate which surface energy was tuned to reach each crystal shape, the new energy value being presented along the morphology. The surface energy (γ) values are in J m^{-2}.

candidates for electronic-based applications. Similarly, the most proposed morphologies have the same potential due to the exposed (001) surfaces. The crystal shapes built from (012), (101), (110), and (100) surfaces present p-type semiconductivity and the same suitability of the bulk form (as a consequence of similar electronic properties), enabling its employment in passive and active components[27]. In this context, we highlight all morphologies from the (6) set, which presents both n-type and p-type semiconductivity.

Thus, different polyhedra with the same exposed surfaces have similar properties as often reported in the literature.[53,110,128–132] Therefore, it is expected that the exposed surfaces in the experimental $LiNbO_3$ morphologies present the same properties calculated from our models.

The DFT prediction of a large number of possible morphologies for $LiNbO_3$ is an innovative approach that clearly allows understanding the morphology control on semiconductor properties.

Conclusion

This manuscript presents a careful DFT/B3LYP investigation of surfaces and morphologies for $LiNbO_3$. The structural and electronic properties for the (110), (012), (101), (100), (001), and (111) surface cuts were extensively depicted. The stability of the $LiNbO_3$ surface decreases in the order (012) > (101) > (110) > (001) > (100) > (111), and the remarkably low surface energy of the (012) surface arises from the high malleability of the Li–O and Nb–O bonds on the surface. The results for the (101) and (001) surfaces indicate that the chemical composition of the termination has more influence on the surface energy than the density of defects. Therefore, O-terminated surfaces are more stable than cation-terminated surfaces with a minor number of vacancies.

In the case of the electronic structure, at least one flat band is observed for all surfaces, the existence of flat bands being a consequence of the presence of vacancies. The (111) surface is an n-type semiconductor, while the other surfaces are p-type semiconductors. The p-type semiconductivity is attached to the major contribution of O states in the VB, favoring the positive charge accumulation on the surface. The calculated properties also suggest that the investigated $LiNbO_3$ surfaces present typical insulator ((012), (110), (101), and (100)), semiconductor ((001)), and conductor ((111)) band gaps. Meanwhile, the evaluation of charge carrier stability points out an excellent charge separation on the surface. In particular, the results indicate the (001) surface as a potential candidate as a photocatalyst.

The predicted morphological set includes both the reported and novel crystalline shapes for $LiNbO_3$. In particular, some morphologies present the n-type and p-type semiconductivity simultaneously.

Finally, the investigation of surface properties indicates that the properties of $LiNbO_3$ in the bulk form, desired for photoacoustic and other acoustic applications, are also observed for the (012), (110), (101), and (100) surfaces, and the morphologies yield a high potential for technological applications. Furthermore, the present manuscript is a comprehensive guide for experimental scientists since the morphologies can be tuned according to the desirable properties.

Conflicts of interest

There are no conflicts to declare.

Acknowledgements

The authors acknowledge support from the CAPES, CNPq, Fundação Araucária (Financing Project 009/2017), LCAD (High-Performance Computing Laboratory) from the State University of Ponta Grossa for your computational facilities acquired by FINEP CT-INFRA/2013, and the "Centro de Computação John David Rogers" (CCJDR-UNICAMP). The authors also acknowledge support from the São Paulo Research Foundation (FAPESP) through grants 2013/07296-2, 2016/23891-6, 2017/26105-4 and 2020/03780-0.

References

1 O. F. Schirmer, O. Thiemann and M. Wöhlecke, Defects in $LiNbO_3$—I. experimental aspects, *J. Phys. Chem. Solids*, 1991, **52**, 185–200.
2 F. Chen, Photonic guiding structures in lithium niobate crystals produced by energetic ion beams, *J. Appl. Phys.*, 2009, **106**, 081101.
3 M. N. Palatnikov, I. V. Biryukova, N. V. Sidorov, A. V. Denisov, V. T. Kalinnikov, P. G. R. Smith and V. Y. Shur, Growth and concentration dependencies of rare-earth doped lithium niobate single crystals, *J. Cryst. Grow.*, 2006, **291**, 390–397.
4 N. A. Benedek and C. J. Fennie, Why Are There So Few Perovskite Ferroelectrics?, *The J. Phys. Chem. C*, 2013, **117**, 13339–13349.
5 M. Nakamura, S. Takekawa, S. Kurimura, K. Kitamura and H. Nakajima, Crystal growth and characterization of titanium-doped near-stoichiometric $LiNbO_3$, *J. Cryst. Grow.*, 2004, **264**, 339–345.
6 S. Yip, Noncentrosymmetric Superconductors, *Annu. Rev. Condens. Matter Phys.*, 2014, **5**, 15–33.
7 S. Cabuk, The nonlinear optical susceptibility and electro-optic tensor of ferroelectrics: first-principle study, *Cent. Eur. J. Phys.*, 2012, **10**, 239–252.
8 L. Arizmendi, Photonic applications of lithium niobate crystals, *Phys. Status Solidi A*, 2004, **201**, 253–283.
9 B. T. Matthias and J. P. Remeika, Ferroelectricity in the Ilmenite Structure, *Phys. Rev.*, 1949, **76**, 1886–1887.
10 Y. Inaguma, A. Aimi, Y. Shirako, D. Sakurai, D. Mori, H. Kojitani, M. Akaogi and M. Nakayama, High-Pressure Synthesis, Crystal Structure, and Phase Stability Relations of a $LiNbO_3$-Type Polar Titanate $ZnTiO_3$ and Its Reinforced Polarity by the Second-Order Jahn–Teller Effect, *J. Am. Chem. Soc.*, 2014, **136**, 2748–2756.

11 K. Nassau, H. J. Levinstein and G. M. Loiacono, Ferroelectric lithium niobate. 1. Growth, domain structure, dislocations and etching, *J. Phys. Chem. Solids*, 1966, **27**, 983–988.
12 K. Nassau, H. J. Levinstein and G. M. Loiacono, Ferroelectric lithium niobate. 2. Preparation of single domain crystals, *J. Phys. Chem. Solids*, 1966, **27**, 989–996.
13 S. C. Abrahams, J. M. Reddy and J. L. Bernstein, Ferroelectric lithium niobate. 3. Single crystal X-ray diffraction study at 24 °C, *J. Phys. Chem. Solids*, 1966, **27**, 997–1012.
14 S. C. Abrahams, H. J. Levinstein and J. M. Reddy, Ferroelectric lithium niobate. 5. Polycrystal X-ray diffraction study between 24° and 1200 °C, *J. Phys. Chem. Solids*, 1966, **27**, 1019–1026.
15 C. Wang, M. Zhang, X. Chen, M. Bertrand, A. Shams-Ansari, S. Chandrasekhar, P. Winzer and M. Lončar, Integrated lithium niobate electro-optic modulators operating at CMOS-compatible voltages, *Nature*, 2018, **562**, 101–104.
16 Z. Chen, Y. Wang, Y. Jiang, R. Kong and H. Hu, Grating coupler on single-crystal lithium niobate thin film, *Opt. Mater.*, 2017, **72**, 136–139.
17 Y.-B. Park, B. Min, K. J. Vahala and H. A. Atwater, Integration of Single-Crystal $LiNbO_3$ Thin Film on Silicon by Laser Irradiation and Ion Implantation–Induced Layer Transfer, *Adv. Mater.*, 2006, **18**, 1533–1536.
18 A. Guarino, G. Poberaj, D. Rezzonico, R. Degl'Innocenti and P. Günter, Electro–optically tunable microring resonators in lithium niobate, *Nat. Photonics*, 2007, **1**, 407–410.
19 F. Chen, Photonic guiding structures in lithium niobate crystals produced by energetic ion beams, *J. Appl. Phys.*, 2009, **106**, 081101.
20 O. F. Schirmer, M. Imlau, C. Merschjann and B. Schoke, Electron small polarons and bipolarons in $LiNbO_3$, *J. Phys.: Condens. Matter*, 2009, **21**, 123201.
21 T. Volk and M. Wöhlecke, *Lithium Niobate: Defects, Photorefraction and Ferroelectric Switching*, Springer-Verlag, Berlin, 2010.
22 J. Deng, J. Wen, Z. Wu and H. Wang, Decay dynamics of laser-induced gratings in $LiNbO_3$:Zn, *Appl. Phys. Lett.*, 1994, **64**, 2622–2624.
23 Y. Kong, S. Wu, S. Liu, S. Chen and J. Xu, Fast photorefractive response and high sensitivity of Zr and Fe codoped $LiNbO_3$ crystals, *Appl. Phys. Lett.*, 2008, **92**, 251107.
24 D. L. Staebler and J. J. Amodei, Coupled-Wave Analysis of Holographic Storage in $LiNbO_3$, *J. Appl. Phys.*, 1972, **43**, 1042–1049.
25 Z. Pei, Q. Hu, Y. Kong, S. Liu, S. Chen and J. Xu, Investigation on p-type lithium niobate crystals, *AIP Adv.*, 2011, **1**, 032171.
26 W. Li, J. Cui, W. Wang, D. Zheng, L. Jia, S. Saeed, H. Liu, R. Rupp, Y. Kong and J. Xu, P-Type Lithium Niobate Thin Films Fabricated by Nitrogen-Doping, *Materials*, 2019, **12**(5), 819.
27 W. Wang, Y. Zhong, D. Zheng, H. Liu, Y. Kong, L. Zhang, R. Romano and J. Xu, p-Type conductivity mechanism and defect structure of nitrogen-doped $LiNbO_3$ from first-principles calculations, *Phys. Chem. Chem. Phys.*, 2020, **22**, 20–27.
28 M. Sumets, Charge transport in $LiNbO_3$-based heterostructures, *J. Nonlinear Opt. Phys. Mater.*, 2017, **26**, 1750011.
29 M. Sumets, G. C. Dannangoda, A. Kostyuchenko, V. Ievlev, V. Dybov and K. S. Martirosyan, Temperature transition of p- to n- type conduction in the $LiNbO_3/Nb_2O_5$ polycrystalline films, *Mater. Chem. Phys.*, 2017, **191**, 35–44.
30 A. El Bachiri, F. Bennani and M. Bousselamti, Dielectric and electrical properties of $LiNbO_3$ ceramics, *J. Asian Ceram. Soc.*, 2016, **4**, 46–54.
31 D. Emin, Dopant- and defect-related small polarons, in: D. Emin (Ed.) *Polarons*, Cambridge University Press, Cambridge, 2012, pp. 43–48.
32 G. Geneste, C. Paillard and B. Dkhil, Polarons, vacancies, vacancy associations, and defect states in multiferroic $${\mathrm{BiFeO}}_{3}$$, *Phys. Rev. B*, 2019, **99**, 024104.
33 T. J. Smart and Y. Ping, Effect of defects on the small polaron formation and transport properties of hematite from first-principles calculations, *J. Phys.: Condens. Matter*, 2017, **29**, 394006.
34 S. V. Levchenko and A. M. Rappe, Influence of Ferroelectric Polarization on the Equilibrium Stoichiometry of Lithium Niobate (0001) Surfaces, *Phys. Rev. Lett.*, 2008, **100**, 256101.
35 S. Sanna and W. G. Schmidt, Lithium niobate X-cut, Y-cut, and Z-cut surfaces from ab initio theory, *Phys. Rev. B*, 2010, **81**, 214116.
36 S. Sanna and W. G. Schmidt, $LiNbO_3$ surfaces from a microscopic perspective, *J. Phys.: Condens. Matter*, 2017, **29**, 413001.
37 K.-y. Hashimoto, H. Asano, T. Omori and M. Yamaguchi, Ultra-Wideband Surface Acoustic Wave Devices Using Cu-Grating/Rotated-YX-$LiNbO_3$-Substrate Structure, *Jpn. J. Appl. Phys.*, 2004, **43**, 3063–3066.
38 A. Krampf, M. Imlau, Y. Suhak, H. Fritze and S. Sanna, Evaluation of similarities and differences of $LiTaO_3$ and LiNbO3 based on high-T-conductivity, nonlinear optical fs-spectroscopy and *ab initio* modeling of polaronic structures, *New J. Phys.*, 2021, **23**, 033016.
39 S. Sanna, R. Hölscher and W. G. Schmidt, Temperature dependent $LiNbO_3$(0001): Surface reconstruction and surface charge, *Appl. Surf. Sci.*, 2014, **301**, 70–78.
40 H. H. Nahm and C. H. Park, First-principles study of microscopic properties of the Nb antisite in $LiNbO_3$: Comparison to phenomenological polaron theory, *Phys. Rev. B*, 2008, **78**, 184108.
41 Y. Li, S. Sanna and W. G. Schmidt, Modeling intrinsic defects in $LiNbO_3$ within the Slater-Janak transition state model, *J. Chem. Phys.*, 2014, **140**, 234113.
42 A. A. Esin, A. R. Akhmatkhanov and V. Y. Shur, Superfast domain wall motion in lithium niobate single crystals. Analogy with crystal growth, *Appl. Phys. Lett.*, 2019, **114**, 192902.
43 A. A. Esin, A. R. Akhmatkhanov and V. Y. Shur, Analogy between growth of crystals and ferroelectric domains. Application of Wulff construction, *J. Cryst. Grow.*, 2019, **526**, 125236.
44 J. Schön, T. Dinges and M. Jansen, Growth of NaBr in the 5–5 Structure Type on $LiNbO_3$: A Feasibility Study, *Z. Naturforsch. B*, 2006, **61b**, 650.

45 N. Zotov, H. Boysen, F. Frey, T. Metzger and E. Born, Cation substitution models of congruent $LiNbO_3$ investigated by X-ray and neutron powder diffraction, *J. Phys. Chem. Solids*, 1994, **55**, 145–152.
46 P. W. Tasker, The stability of ionic crystal surfaces, *J. Phys. C-Solid State Phys.*, 1979, **12**, 4977–4984.
47 Y. Dai, Q. Gao, C. Cui, L. Yang, C. Li and X. Li, Role of ferroelectric/ferromagnetic layers on the ferroelectric properties of magnetoelectric composite films derived by chemical solution deposition, *Mater. Res. Bull.*, 2018, **99**, 424–428.
48 J.-Q. Dai, J.-W. Xu and J.-H. Zhu, Thermodynamic Stability of $BiFeO_3$ (0001) Surfaces from ab Initio Theory, *ACS Appl. Mater. Interfaces*, 2017, **9**, 3168–3177.
49 M. M. Teixeira, R. C. de Oliveira, M. C. Oliveira, R. A. Pontes Ribeiro, S. R. de Lazaro, M. S. Li, A. J. Chiquito, L. Gracia, J. Andrés and E. Longo, Computational Chemistry Meets Experiments for Explaining the Geometry, Electronic Structure, and Optical Properties of Ca10V6O25, *Inorg. Chem.*, 2018, **57**, 15489–15499.
50 R. A. P. Ribeiro, S. R. de Lazaro, L. Gracia, E. Longo and J. Andrés, Theoretical approach for determining the relation between the morphology and surface magnetism of Co_3O_4, *J. Magn. Magn. Mater.*, 2018, **453**, 262–267.
51 R. A. P. Ribeiro, J. Andrés, E. Longo and S. R. Lazaro, Magnetism and multiferroic properties at $MnTiO_3$ surfaces: A DFT study, *Appl. Surf. Sci.*, 2018, **452**, 463–472.
52 R. A. P. Ribeiro, E. Longo, J. Andrés and S. R. de Lazaro, A DFT investigation of the role of oxygen vacancies on the structural, electronic and magnetic properties of $ATiO_3$ (A = Mn, Fe, Ni) multiferroic materials, *Phys. Chem. Chem. Phys.*, 2018, **20**, 28382–28392.
53 R. A. P. Ribeiro, L. H. S. Lacerda, E. Longo, J. Andrés and S. R. de Lazaro, Towards enhancing the magnetic properties by morphology control of $ATiO_3$ (A = Mn, Fe, Ni) multiferroic materials, *J. Magn. Magn. Mater.*, 2019, **475**, 544–549.
54 M. C. Oliveira, R. A. P. Ribeiro, L. Gracia, S. R. de Lazaro, M. de Assis, M. Oliva, I. L. V. Rosa, M. F. D. C. Gurgel, E. Longo and J. Andrés, Experimental and theoretical study of the energetic, morphological, and photoluminescence properties of $CaZrO_3$:Eu^{3+}, *CrystEngComm*, 2018, **20**, 5519–5530.
55 L. H. d. S. Lacerda and S. R. de Lazaro, Theoretical investigation on the surface and morphological properties of lead nickelate multiferroics: vacancy dependency, *J. Mater. Sci.*, 2020, **55**, 6875–6890.
56 K. Reuter and M. Scheffler, Composition and structure of the RuO_2 surface in an O_2 and CO environment: Implications for the catalytic formation of CO_2, *Phys. Rev. B*, 2003, **68**, 045407.
57 K. Reuter and M. Scheffler, Composition, structure, and stability of RuO_2 as a function of oxygen pressure, *Phys. Rev. B*, 2001, **65**, 035406.
58 Q. Cai, J.-g. Wang, Y. Wang and D. Mei, First-Principles Thermodynamics Study of Spinel $MgAl_2O_4$ Surface Stability, *J. Phys. Chem. C*, 2016, **120**, 19087–19096.
59 A. D. Becke, Perspective: Fifty years of density-functional theory in chemical physics, *J. Chem. Phys.*, 2014, **140**, 18A301–318A320.
60 R. Dovesi, A. Erba, R. Orlando, C. M. Zicovich-Wilson, B. Civalleri, L. Maschio, M. Rérat, S. Casassa, J. Baima, S. Salustro and B. Kirtman, Quantum-mechanical condensed matter simulations with CRYSTAL, *Wiley Interdiscip. Rev.: Comput. Mol. Sci.*, 2018, **8**, e1360–1336.
61 M. D. Towler, N. L. Allan, N. M. Harrison, V. R. Saunders, W. C. Mackrodt and E. Aprà, Ab initio study of MnO and NiO, *Phys. Rev. B*, 1994, **50**, 5041–5054.
62 A. M. Ferrari and C. Pisani, An *ab Initio* Periodic Study of NiO Supported at the Pd (100) Surface. Part 1: The Perfect Epitaxial Monolayer, *J. Phys. Chem. B*, 2006, **110**, 7909–7917.
63 G. Sophia, P. Baranek, C. Sarrazin, M. Rerat, R. Dovesi, Systematic influence of atomic substitution on the phase diagram of ABO3 ferroelectric perovskites. (Unpublished work), in, 2013.
64 H. J. Monkhorst and J. D. Pack, Special points for Brillouin-zone integrations, *Phys. Rev. B*, 1976, **13**, 5188–5192.
65 C. Pisani, R. Dovesi and C. Roetti, *Hartree–Fock ab initio Treatment of Crystalline Systems*, Springer Berlin Heidelberg, 1988.
66 H. J. Donnerberg, S. M. Tomlinson and C. R. A. Catlow, Defects in LiNbO3—II. Computer simulation, *J. Phys. Chem. Solids*, 1991, **52**, 201–210.
67 N. A. Benedek and C. J. Fennie, Why Are There So Few Perovskite Ferroelectrics?, *J. Phys. Chem. C*, 2013, **117**, 13339–13349.
68 T. Varga, A. Kumar, E. Vlahos, S. Denev, M. Park, S. Hong, T. Sanehira, Y. Wang, C. J. Fennie, S. K. Streiffer, X. Ke, P. Schiffer, V. Gopalan and J. F. Mitchell, Coexistence of Weak Ferromagnetism and Ferroelectricity in the High Pressure $LiNbO_3$-Type Phase of $FeTiO_3$, *Phys. Rev. Lett.*, 2009, **103**, 047601.
69 C. J. Fennie, Ferroelectrically Induced Weak Ferromagnetism by Design, *Phys. Rev. Lett.*, 2008, **100**, 167203.
70 N. Chaniotakis and N. Sofikiti, Novel semiconductor materials for the development of chemical sensors and biosensors: A review, *Anal. Chim. Acta*, 2008, **615**, 1–9.
71 K. J. Yu, Z. Yan, M. Han and J. A. Rogers, Inorganic semiconducting materials for flexible and stretchable electronics, *npj Flexible Electronics*, 2017, **1**, 4.
72 M. Kuno, *Introductory Nanoscience: Physical and Chemical Concept*, Garland Science: Taylor & Francis Group, Oxford, 2011.
73 L. H. S. Lacerda and S. R.d. Lazaro, Ba-doped ZnO Materials: A DFT simulation to investigate the doping effect on ferroelectricity, *Quim. Nova*, 2016, **39**, 261–266.
74 L. H. S. Lacerda and S. R. de Lazaro, A theoretical investigation of the Zn-doping influence on structural and electronic properties of $BaTiO_3$, *Solid State Ionics*, 2016, **297**, 36–42.
75 L. H. S. Lacerda and S. R. de Lazaro, Density Functional Theory investigation of rhombohedral multiferroic oxides for photocatalytic water splitting and organic photodegradation, *J. Photochem. Photobiol., A*, 2020, **400**, 112656.
76 Q. Zhou, Y. Liu, W. Ju, Q. Zhang and J. Li, Exploring the effect of dopant (Si, P, S, Ge, Se, and Sb) in arsenene: A DFT study, *Phys. Lett. A*, 2020, **384**, 126146.

77 A. Majorana and R. M. Pidatella, A Finite Difference Scheme Solving the Boltzmann–Poisson System for Semiconductor Devices, *J. Comput. Phys.*, 2001, **174**, 649–668.
78 F. Oba and Y. Kumagai, Design and exploration of semiconductors from first principles: A review of recent advances, *Appl. Phys. Express*, 2018, **11**, 060101.
79 K. Yim, Y. Youn, M. Lee, D. Yoo, J. Lee, S. H. Cho and S. Han, Computational discovery of p-type transparent oxide semiconductors using hydrogen descriptor, *npj Comput. Mater.*, 2018, **4**, 17.
80 C. Freysoldt, B. Grabowski, T. Hickel, J. Neugebauer, G. Kresse, A. Janotti and C. G. Van de Walle, First-principles calculations for point defects in solids, *Rev. Mod. Phys.*, 2014, **86**, 253–305.
81 Y. Kumagai, M. Choi, Y. Nose and F. Oba, First-principles study of point defects in chalcopyrite $SnSnP_2$, *Phys. Rev. B*, 2014, **90**, 125202.
82 C. Persson, Y.-J. Zhao, S. Lany and A. Zunger, n-type doping of $CuInSe_2$ and $CuGaSe_2$, *Phys. Rev. B*, 2005, **72**, 035211.
83 R. Sun, M. K. Y. Chan, S. Kang and G. Ceder, Intrinsic stoichiometry and oxygen-induced p-type conductivity of pyrite FeS_2, *Phys. Rev. B*, 2011, **84**, 035212.
84 A. Boltasseva and H. A. Atwater, Low-Loss Plasmonic Metamaterials, *Science*, 2011, **331**, 290.
85 G. K. H. Madsen and D. J. Singh, BoltzTraP. A code for calculating band-structure dependent quantities, *Comput. Phys. Commun.*, 2006, **175**, 67–71.
86 A. Dhar and A. Mansingh, Optical properties of reduced lithium niobate single crystals, *J. Appl. Phys.*, 1990, **68**, 5804–5809.
87 R. K. Nath, M. F. M. Zain and A. A. H. Kadhum, Artificial Photosynthesis using $LiNbO_3$ as Photocatalyst for Sustainable and Environmental Friendly Construction and Reduction of Global Warming: A Review, *Catal. Rev.*, 2014, **56**, 175–186.
88 A. Dasmahapatra, L. E. Daga, A. J. Karttunen, L. Maschio and S. Casassa, The Key Role of Defects in Thermoelectric Performance of TiMSn(M = Ni, Pd, Pt) Half-Heusler Alloys, *J. Phys. Chem. C*, 2020, **124**, 14997.
89 N. Iyi, K. Kitamura, Y. Yajima, S. Kimura, Y. Furukawa and M. Sato, Defect Structure Model of MgO-Doped $LiNbO_3$, *J. Solid State Chem.*, 1995, **118**, 148–152.
90 Y. Wang, X. Y. Zhou, Z. Chen, B. Cai, Z. Z. Ye, C. Y. Gao and J. Y. Huang, Synthesis of cubic $LiNbO_3$ nanoparticles and their application in vitro bioimaging, *Appl. Phys. A*, 2014, **117**, 2121–2126.
91 J. Yu, P. Zhou and Q. Li, New insight into the enhanced visible-light photocatalytic activities of B-, C- and B/C-doped anatase TiO_2 by first-principles, *Phys. Chem. Chem. Phys.*, 2013, **15**, 12040–12047.
92 P. Zhou, J. Yu and Y. Wang, The new understanding on photocatalytic mechanism of visible-light response NS codoped anatase TiO_2 by first-principles, *Appl. Catal., B*, 2013, **142–143**, 45–53.
93 X. Ma, Y. Dai, M. Guo and B. Huang, The Role of Effective Mass of Carrier in the Photocatalytic Behavior of Silver Halide-Based Ag@AgX (X = Cl, Br, I): A Theoretical Study, *Chem. Phys. Chem.*, 2012, **13**, 2304–2309.
94 G. B. Soares, R. A. P. Ribeiro, S. R. de Lazaro and C. Ribeiro, Photoelectrochemical and theoretical investigation of the photocatalytic activity of TiO_2:N, *RSC Adv.*, 2016, **6**, 89687–89698.
95 N. Gao, C. Quan, Y. Ma, Y. Han, Z. Wu, W. Mao, J. Zhang, J. Yang, X.a. Li and W. Huang, Experimental and first principles investigation of the multiferroics $BiFeO_3$ and $Bi_{0.9}Ca_{0.1}FeO_3$: Structure, electronic, optical and magnetic properties, *Phys. B*, 2016, **481**, 45–52.
96 Y. Gu, J. Zhao, W. Zhang, H. Zheng, L. Liu and W. Chen, Structural transformation and multiferroic properties of Sm and Ti co-doped $BiFeO_3$ ceramics with Fe vacancies, *Ceram. Int.*, 2017, **43**, 14666–14671.
97 A. Das, S. De, S. Bandyopadhyay, S. Chatterjee and D. Das, Magnetic, dielectric and magnetoelectric properties of $BiFeO_3$-$CoFe_2O_4$ nanocomposites, *J. Alloys Compd.*, 2017, **697**, 353–360.
98 T. Murtaza, J. Ali, M. S. Khan and K. Asokan, Structural, electrical and magnetic properties of multiferroic $BiFeO_3$–$SrTiO_3$ composites, *J. Mater. Sci.: Mater. Electron.*, 2018, **29**, 2110–2119.
99 J. Silva, A. Reyes, H. Esparza, H. Camacho and L. Fuentes, BiFeO3: A Review on Synthesis, Doping and Crystal Structure, *Integr. Ferroelectr.*, 2011, **126**, 47–59.
100 T. Jing, Y. Dai, X. Ma, W. Wei and B. Huang, Electronic Structure and Photocatalytic Water-Splitting Properties of $Ag_2ZnSn(S_{1-x}Se_x)_4$, *J. Phys. Chem. C*, 2015, **119**, 27900–27908.
101 X. Li, C. He, D. Dai, S. Zuo, X. Yan, C. Yao and C. Ni, Nanomineral induced nonlinear optical $LiNbO_3$ with abundant oxygen vacancies for photocatalytic nitrogen fixation: boosting effect of polarization, *Appl. Nanosci.*, 2020, **10**, 3477.
102 R.-z. Zhang, X.-y. Hu, P. Guo and C.-l. Wang, Thermoelectric transport coefficients of n-doped $CaTiO_3$, $SrTiO_3$ and $BaTiO_3$: A theoretical study, *Phys. B*, 2012, **407**, 1114–1118.
103 A. J. Cohen, P. Mori-Sanchez and W. Yang, Fractional charge perspective on the band gap in density-functional theory, *Phys. Rev. B: Condens. Matter Mater. Phys.*, 2008, **77**, 115123.
104 C. Yue, X. Lu, J. Zhang, F. Huang and J. Zhu, Ferroelectric surface chemistry: First-principles study of adsorption on the stoichiometric $LiNbO_3$ (0001) surface, *Phys. Rev. B*, 2019, **100**, 245432.
105 J. Picard and R. Cerf, *The Wulff Crystal in Ising and Percolation Models: Ecole d'Eté de Probabilités de Saint-Flour XXXIV - 2004*, Springer Berlin Heidelberg, 2006.
106 G. Wulff, Zur Frage der Geschwindigkeit des Wachstums und der Auflösung der Krystallflagen, *Z. Krystallogr. Mineral.*, 1901, **34**, 449–530.
107 G. D. Barmparis, Z. Lodziana, N. Lopez and I. N. Remediakis, Nanoparticle shapes by using Wulff constructions and first-principles calculations, *Beilstein J. Nanotechnol.*, 2015, **6**, 361–368.
108 J. Andrés, L. Gracia, A. F. Gouveia, M. M. Ferrer and E. Longo, Effects of surface stability on the morphological transformation of metals and metal oxides as investigated by first-principles calculations, *Nanotechnology*, 2015, **26**, 405703.

109 L. D. Marks and L. Peng, Nanoparticle shape, thermodynamics and kinetics, *J. Phys.: Condens. Matter*, 2016, **28**, 053001.
110 L. H. D. S. Lacerda and S. R. de Lazaro, Surface and morphology investigation of $FeCrO_3$ material in ilmenite-, corundum- and lithium niobate- polymorphs, *Surf. Interfaces*, 2021, **22**, 100837.
111 K. C. L. Bauerfeind, R. Roß and T. Bredow, Theoretical Study of Polar Spinel Surfaces: Effect of Termination and Cation Inversion on Structure and Stability, *J. Phys. Chem. C*, 2020, **124**, 28520–28530.
112 M. A. Fakhri, N. H. Numan, Z. S. Alshakhli, M. A. Dawood, A. W. Abdulwahhab, F. G. Khalid, U. Hashim and E. T. Salim, Physical investigations of nano and micro lithium-niobate deposited by spray pyrolysis technique, *AIP Conf. Proc.*, 2018, **2045**, 020015.
113 C. Debnath, S. Kar, S. Verma and K. S. Bartwal, Investigations on crystalline structure and optical band gap of nearly stoichiometric $LiNbO_3$ nanoparticles, *Opt. Mater.*, 2014, **37**, 804–809.
114 V. Bouquet, E. R. Leite, E. Longo and J. A. Varela, Structural and surface morphology characterizations of oriented $LiNbO_3$ thin films grown by polymeric precursor method, *J. Eur. Ceram. Soc.*, 1999, **19**, 1447–1451.
115 M. A. Fakhri, N. H. Numan, M. H. Kheder, B. A. Badr, F. G. Khalid, U. Hashim, E. T. Salim and Z. T. Salim, Epitaxial growth of photonic $LiNbO_3$ nano crystals and structural studies using for waveguides, *AIP Conf. Proc.*, 2018, **2045**, 020019.
116 M. Liu, D. Xue and K. Li, Soft-chemistry synthesis of $LiNbO_3$ crystallites, *J. Alloys Compd.*, 2008, **449**, 28–31.
117 R. Sumang, F. Sutamma, S. Chootin and T. Bongkarn, Influence of Firing Temperatures on Crystal Structure and Microstructure of $LiNbO_3$ Ceramics, *Integr. Ferroelectr.*, 2013, **149**, 1–8.
118 M. Jelínek, V. Havránek, J. Remsa, T. Kocourek, A. Vincze, J. Bruncko, V. Studnička and K. Rubešová, Composition, XRD and morphology study of laser prepared $LiNbO_3$ films, *Appl. Phys. A*, 2013, **110**, 883–888.
119 M. A. Fakhri, E. T. Salim, A. W. Abdulwahhab, U. Hashim, M. A. Munshid and Z. T. Salim, The effect of annealing temperature on optical and photoluminescence properties of $LiNbO_3$, *Surf. Rev. Lett.*, 2019, **26**, 1950068.
120 Y. Lin, S. Cui, Y. M. Li and X. F. Ren, Low temperature synthesis of $LiNbO_3$ powder with different fluxes, *Mater. Technol.*, 2008, **23**, 23–26.
121 J. Yu and X. Liu, Hydrothermal synthesis and characterization of $LiNbO_3$ crystal, *Mater. Lett.*, 2007, **61**, 355–358.
122 X. Zhang, J. Yuan, P. Xia, G. Li, Y. Yu, X. Zhu, Z. Xiong, H. Yu and Y. Xie, Controllable synthesis of $LiNbO_3$ micro-octahedrons and micro-cubes via a molten-salt process, *Ceram. Int.*, 2018, **44**, 22874–22879.
123 S. Solanki, T.-C. Chong and X. Xu, Flux growth and morphology study of stoichiometric lithium niobate crystals, *J. Cryst. Grow.*, 2003, **250**, 134–138.
124 Z.-Y. Zhang, Y.-y. Zhu, H.-f. Wang, L.-c. Wang, S.-n. Zhu and N.-b. Ming, Domain inversion in LiNbO3 and LiTaO3 induced by proton exchange, *Phys. B*, 2007, **398**, 151–158.
125 Y. Al-Douri, C. H. Voon, A. Bouhemadou and M. Ameri, Spin-coating technique to investigate structural and optical properties of nano and micro cubic-like photonic $LiNbO_3$ under annealing temperature effect, *Optik*, 2018, **172**, 519–525.
126 F. Veignant, M. Gandais, P. Aubert and G. Garry, Epitaxial growth of $LiNbO_3$ on $\alpha Al_2O_3(0001)$, *Thin Solid Films*, 1998, **336**, 163–167.
127 D. Sun, J. Xiao, L. Zhang, Y. Hang, S. Zhu, A. Wang and S. Yin, Study on the growth facets and ferroelectric domains in near-stoichiometric $LiNbO_3$ crystals, *J. Cryst. Grow.*, 2004, **262**, 240–245.
128 W. Wang, S. Wang, D. He and J.-A. Xu, Pressure induced phase transition of $PbNiO_3$ from $LiNbO_3$-type to perovskite, *Solid State Commun.*, 2014, **196**, 8–12.
129 F. Namvar, F. Beshkar and M. Salavati-Niasari, Novel microwave-assisted synthesis of leaf-like $MnMoO_4$ nanostructures and investigation of their photocatalytic performance, *J. Mater. Sci.: Mater. Electron.*, 2017, **28**, 7962–7968.
130 C. Zhang, D. Wu, L. Shi, Y. Zhu, D. Xiong, S. Xu, R. Huang, R. Qi, W. Zhang, L. Wang and P. K. Chu, Manganese molybdate nanoflakes on silicon microchannel plates as novel nano energetic material, *R. Soc. Open Sci.*, 2017, **4**, 171229.
131 F. Nti, D. A. Anang and J. I. Han, Facile room temperature synthesis and application of $MnMoO_4{\cdot}0.9H_2O$ as supercapacitor electrode material, *Mater. Lett.*, 2018, **217**, 146–150.
132 G. Harichandran, S. Radha, P. Divya and J. Yesuraj, Facile morphology-controlled synthesis of nanostructured $MnMoO_4$ nanorods as an advance electrode material for supercapacitor application, *J. Mater. Sci.: Mater. Electron.*, 2020, **31**, 1646–1653.